Metal Halide Perovskites for Solar-to-Chemical Fuel Conversion

*Jie Chen, Chunwei Dong, Hicham Idriss, Omar F. Mohammed, and Osman M. Bakr**

This review article presents and discusses the recent progress made in the stabilization, protection, improvement, and design of halide perovskite-based photocatalysts, photoelectrodes, and devices for solar-to-chemical fuel conversion. With the target of water splitting, hydrogen iodide splitting, and CO_2 reduction reactions, the strategies established for halide perovskites used in photocatalytic particle-suspension systems, photoelectrode thin-film systems, and photovoltaic-(photo)electrocatalysis tandem systems are organized and introduced. Moreover, recent achievements in discovering new and stable halide perovskite materials, developing protective and functional shells and layers, designing proper reaction solution systems, and tandem device configurations are emphasized and discussed. Perspectives on the future design of halide perovskite materials and devices for solar-to-chemical fuel conversion are provided. This review may serve as a guide for researchers interested in utilizing halide perovskite materials for solar-to-chemical fuel conversion.

1. Introduction

Efficient conversion of solar energy to chemical fuels on a scale on par with the energy supplied from conventional fossil fuels is a promising yet challenging pathway to realizing a sustainable carbon-neutral society.[1–7] The main chemical energy carriers in this pathway are H_2 and various C_1–C_3 compounds, which have either high energy densities or versatile applications in industry but require thermodynamically uphill water splitting or CO_2 reduction reactions to be produced.[5–9] To date, several solar-to-chemical fuel conversion systems, including photocatalyst particle-suspension, photoelectrode thin-film, and photovoltaic (PV)-electrocatalysis systems, have been

developed to meet the requirements of certain reactions and have been optimized for practical use.[5,8] Although the reaction system configurations vary, one of the key elements to a solar-to-chemical fuel conversion system is the semiconductor material, which converts solar energy to excited electrons and holes that then separate to drive uphill reduction and oxidation reactions.[2,10,11]

Metal halide perovskites with a general formula of ABX_3 (**Figure 1**a), where typically A is methylammonium (MA), formamidinium (FA) or Cs; B is Pb or Sn; and X is Cl, Br or I, have recently emerged as a promising class of high-performance semiconductors since the first solar cell involving $MAPbI_3$.[12] These perovskites have remarkable photophysical, optical, and transport properties, such as long charge carrier lifetimes and low trap densities,[13,14] long electron and hole diffusion lengths,[15–17] large absorption coefficients,[18,19] and a widely tunable bandgap that enables light harvesting from UV to near IR spectral range[20,21] (Figure 1b). More importantly, the band positions of most halide perovskites satisfy the thermodynamic requirements for water and CO_2 reduction, as shown in Figure 1c.

By virtue of their impressive photophysical properties, halide perovskites have been successfully used in various optoelectronic devices, including solution-processed solar cells with power conversion efficiency (PCE) exceeding 25%,[22–25] low-threshold lasers,[26,27] bright light-emitting diodes[28–30] and sensitive photo- and X-ray detectors.[31–34] These successes have also motivated the development of solar-to-chemical fuel conversion systems based on halide perovskites. However, halide perovskites generally have low formation enthalpy, which intrinsically makes them easy to form as well as easy to be damaged.[35] Upon an external stimuli such as moisture and polar solvent, oxygen, heat, and irradiation, halide perovskites are easily decomposed to its binary halide components (for example, $MAPbI_3 \rightarrow MAI + PbI_2$). This instability of halide perovskites has limited their study and applications. To date, substantive efforts have been made to enable halide perovskites for solar-to-chemical fuel conversion. For example, halide perovskites powder suspensions were used in non-aqueous solutions for CO_2 reduction.[36] Moreover, halide perovskite photoelectrodes were protected by functional layers for H_2O reduction[37] and CO_2 reduction.[38] In another instance, perovskite photovoltaics were used to drive electrocatalytic water splitting or CO_2 reduction by connecting an isolated photovoltaic

Dr. J. Chen, C. W. Dong, Prof. O. F. Mohammed, Prof. O. M. Bakr
Division of Physical Science and Engineering (PSE)
King Abdullah University of Science and Technology (KAUST)
Thuwal 23955-6900, Saudi Arabia
E-mail: osman.bakr@kaust.edu.sa
Dr. J. Chen, C. W. Dong, Prof. O. M. Bakr
KAUST Catalysis Center
Thuwal 23955-6900, Saudi Arabia
Prof. H. Idriss
Fundamental Catalysis
Centre for Research and Development (CRD)
SABIC
Thuwal 23955-6900, Saudi Arabia

The ORCID identification number(s) for the author(s) of this article can be found under https://doi.org/10.1002/aenm.201902433.

**ADVANCED
SCIENCE NEWS**

www.advancedsciencenews.com

**ADVANCED
ENERGY
MATERIALS**

www.advenergymat.de

cell to an electrocatalysis cell.[8] Despite this progress, the field is at its infancy and there is still much room for innovation in designing target reaction systems as well as in enhancing the stability and efficiency of halide perovskites for solar-to-chemical fuel conversion.

In this review, we summarize the advancements made to date in the development of halide perovskites for solar-to-chemical fuel conversion. The reactions involved in this process are water splitting, hydrogen iodide splitting, and CO_2 reduction. We classify and introduce the achievements made in incorporating halide perovskites into photocatalyst particle-suspension systems, photoelectrode thin-film systems, and photovoltaic-(photo)electrocatalytic systems. We also introduce and discuss the syntheses and modification strategies established for yielding stable and efficient halide perovskites as well as the design of reaction system configurations. We hope that this work will inspire researchers to translate the benefits afforded by the remarkable photophysical properties of halide perovskites into highly efficient, stable, and selective solar-driven chemical fuel production.

2. Photocatalytic Particle-Suspension Systems

In 1979, Bard designed the first photocatalyst particle-suspension system for water splitting[39] after Fujishima and Honda had discovered the Honda–Fujishima effect in the early 1970s.[40] A photocatalytic reaction is carried out in a closed gas-circulation cell containing semiconductor particles as the photocatalysts, water as the proton or oxygen source, sacrificial reagents (if necessary) for half oxidation or reduction reactions, and dissolved CO_2 (if the system is meant for CO_2 reduction).

Upon light irradiation, a semiconductor photocatalyst generates charge carriers (electrons and holes), see process (1) in **Figure 2**. Here, the energy of the incident light must exceed the bandgap energy of the semiconductor to allow for effective excitation. As the ΔG^0 values for water splitting and CO_2 reduction are 237 and 259 kJ mol^{-1} (taking the conversion of CO_2 to CO as an example), respectively, a theoretical bandgap of at least 1.34 eV (corresponds to 954 nm) is required. Photoexcited charge carriers then migrate to the reactive sites for certain reactions, as shown in process (2) of Figure 2. Concomitant recombination, including bulk and surface recombination, process (2′), of the charge carriers (electron and hole) will also occur radiatively and/or nonradiatively, releasing photons or thermal energy. The electrons and holes reaching the reactive sites then undergo an electrochemical catalytic process to produce chemical fuels. Thermodynamically, such a process requires the electron potential (conduction band, CB potential of the semiconductor) to be more negative than 0 V versus normal hydrogen electrode (NHE) for reducing H$^+$ to H$_2$ (−0.107 V vs NHE for CO_2 to CO, pH = 0), and the hole potential (valence band, VB potential) must be more positive than the oxidation potential of H_2O/O_2 (1.23 V vs NHE, pH = 0). Generally, halide perovskites thermodynamically favor both the reduction and oxidation reactions, as their CB and VB straddle the water/CO_2 reduction and water oxidation potentials (Figure 1c). However, the complexity of the overall catalytic cycle requires the use of multiple components for kinetic reasons in addition

to the above basic thermodynamic requirement in a real-experimental scenario. In this case, electrocatalysts (ECs) such as Pt, MoS_2, RuO_2, and others are usually needed to extract electrons/holes from the semiconductors, as well as to promote the kinetics for the catalytic reactions.

Jie Chen obtained his bachelor degree in Applied Chemistry from Xi'an Jiaotong University in 2011 and his Ph.D. degree in Power engineering and engineering Thermophysics from Xi'an Jiaotong University in 2017. During 2015–2017, he worked as a joint student in Department of Chemistry at UW-Madison. He is currently a postdoctoral researcher working with Prof. Osman Bakr in the KAUST Catalysis Center. His research interests focus on functional nanomaterials for catalysis and optoelectronics applications.

Chunwei Dong obtained his bachelor degree in Chemistry from Jilin University in 2013 and his Ph.D. degree in Polymeric Chemistry and Physics under the supervision of Prof. Hao Zhang from Jilin University in 2018. He is currently a postdoctoral researcher working with Prof. Osman Bakr in KAUST Catalysis Center. His research interests focus on the synthesis of functional nanomaterials for catalytic applications.

Osman M. Bakr holds a B.Sc. in Materials Science and Engineering from MIT (2003) as well as M.S. and Ph.D. in Applied Physics from Harvard University (2009). He is currently Professor of Materials Science and Engineering at KAUST, Saudi Arabia. His research group focuses on the study of hybrid organic–inorganic materials; particularly, advancing their synthesis and self-assembly for applications in optoelectronics and catalysis.
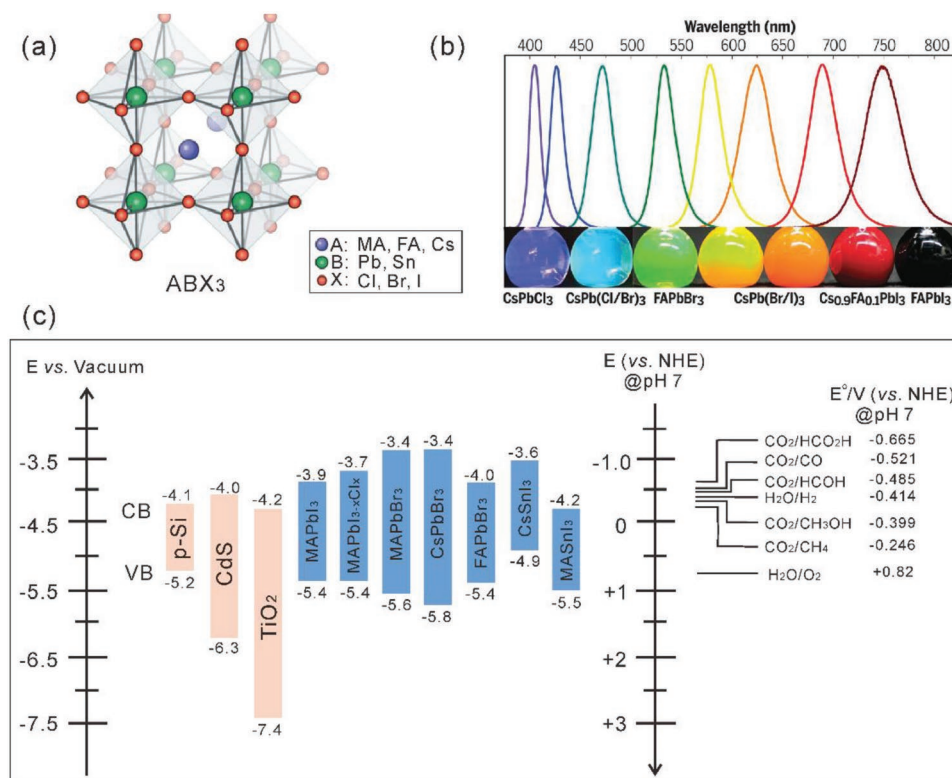
Figure 1. a) General crystal structure of the 3D halide perovskite ABX_3. Reproduced with permission.[20] Copyright 2019, Nature Publishing Group. b) Photoluminescence spectra and corresponding photographs of composition-tuned halide perovskite nanocrystals. Reproduced with permission.[21] Copyright 2017, AAAS. c) Conduction band (CB) and valence band (VB) potentials of representative semiconductors (p-Si, CdS, TiO_2) and halide perovskites for solar-to-chemical fuel conversion. The relative potentials of the CO_2 and water redox couples at pH 7 are plotted versus vacuum (left) and normal hydrogen electrode (NHE) (right).

For photocatalyst particle-suspension systems, water/moisture instability issues associated with halide perovskites must be considered. Halide perovskites generally cannot resist water, even though some strategies can render them stable against a certain percentage of humidity.[41,42] To this end, researchers have expended great efforts by developing water-stable perovskite and structures, discovering proper proton sources (e.g.,

Figure 2. An illustration of charge transfer reactions that may occur at the surface and in the bulk of a semiconductor photocatalyst.

hydrogen iodide, HI) other than water, and dispersing halide perovskite in non-aqueous solutions for CO_2 reduction.

2.1. Water-Stable Halide Perovskites and Structures

Most of the reported halide perovskites have been recognized to dissolve like a salt in water. Encouragingly, Ju et al. have reported that $DMASnI_3$ (DMA = $CH_3NH_2CH_3^+$), although not in a typical 3D perovskite structure, can be suspended in deionized (DI) water for photocatalytic water splitting H_2 production with a rate of 0.64 µmol h^{-1} (200 mg catalysts) for at least 5 h (**Figure 3**a).[43] This is an interesting work in which a halide perovskite has been reported to for water splitting, although the precise mechanism underlying this water stability is not yet clear. $ADPb_2Cl_5$ (AD = acridine), with a bandgap of 2.06 eV, was also reported to be water-stable; however, the material was not used for solution-phase photocatalytic reactions.[44] $ADPb_2Cl_5$ is stable because the large steric hindrance exhibited by AD cations distributed between the rigid lead chloride inorganic matrices could effectively prevent erosion by water.

Strategies for protecting and functionalizing halide perovskites for photocatalysis have also been developed. One instant idea is to coat perovskite nanocrystals with a shell that is water-resistant, stable, and photocatalytically active. Li et al. have coated colloidal $CsPbBr_3$ with a TiO_2 shell by hydrolysis
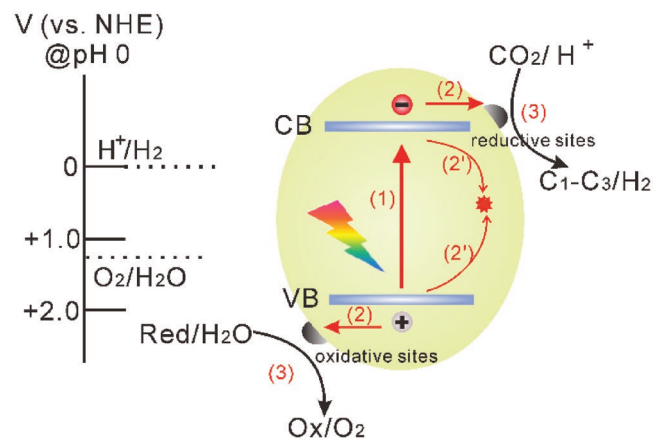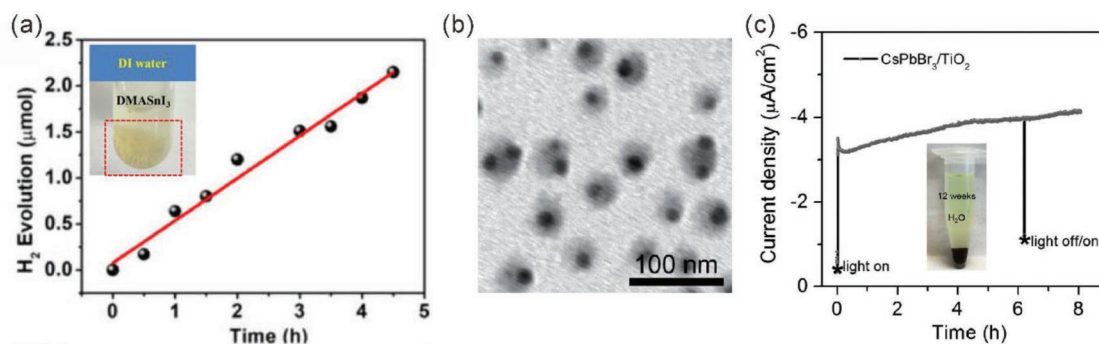
Figure 3. a) Hydrogen production over $DMASnI_3$ crystals in DI water. Inset shows $DMASnI_3$ crystals dispersed in DI water. Reproduced with permission.[43] Copyright 2018, Wiley. b) A TEM image of $CsPbBr_3@TiO_2$ core–shell nanocrystals (NCs). c) Controlled potential electrolysis of $CsPbBr_3@TiO_2$ NC electrode in neutral water over 8 h. Inset shows a photograph of $CsPbBr_3@TiO_2$ in water for 12 weeks. b,c) Reproduced with permission.[45] Copyright 2018, Wiley.

and calcination of a titanium precursor (Figure 3b).[45] The $CsPbBr_3@TiO_2$ NCs were very stable and exhibited excellent water stability for more than 12 weeks, with size, morphology, and crystallinity unchanged. Remarkably, the $CsPbBr_3@TiO_2$ NCs maintained a relatively constant photocurrent over 8 h under real-world photoelectric test conditions in water (Figure 3c). Using a zeolitic imidazolate framework (ZIF) as the shell, Kong et al. have fabricated $CsPbBr_3@ZIF$ core–shell structures by in situ growth of ZIF on $CsPbBr_3$ quantum dots (QDs).[46] The $CsPbBr_3@ZIF$ composites were active and stable for the photocatalytic CO_2 reduction in the presence of CO_2 and H_2O vapor and exhibited electron consumption rates of 15.5 and 29.6 $\mu mol\ g^{-1}\ h^{-1}$ for $CsPbBr_3@ZIF-8$ and $CsPbBr_3@ZIF-67$, respectively. Other perovskite@shell structures, such as $CsPbBr_3@SiO_2$[47] and $CsPbBr_3@Al_2O_3$,[48,49] have also been successfully synthesized; however, they have not been used as described above and might not be active for photocatalytic reactions because the SiO_2 or Al_2O_3 layers are not photocatalytic active.

2.2. Using Hydrogen Iodide (HI) Solution Other than Water

HI was first pointed out by Park et al. as a better choice than water for providing protons for H_2 production when employing $MAPbI_3$ as the photocatalyst.[50] $MAPbI_3$ is stable in a $MAPbI_3$-saturated aqueous HI solution because of the dynamic equilibrium between $MAPbI_3$ and HI. By dissolving a series of amounts of $MAPbI_3$ in HI, Park et al. obtained corresponding solubility data and proposed a dynamic equilibrium model for the $MAPbI_3$ to be stable in HI solution (**Figure 4**a,b). Moreover, the authors identified the conditions for the formation of stable $MAPbI_3$ precipitates in aqueous solution by controlling the I^- and H^+ concentrations ($[I^-] \leq [H^+]$, pH ≤ -0.5, $-\log[I^-] \leq -0.4$). In aqueous HI solution, the $MAPbI_3$ powders could efficiently split HI into H_2 and I_3^- under visible-light irradiation according to a mechanism that is similar to water splitting (Figure 4c,d), and a solar HI splitting efficiency of 0.81% was achieved when using Pt as a cocatalyst.

HI solution has been widely adopted by other researchers since the work of Park et al. For example, Huang and co-workers used HI and HBr/HI mixed solutions to test a

modified $MAPbI_3/rGO$ material[51] and the mixed halide perovskites $MAPbBr_{3-x}I_x$[52] and $CsPbBr_{3-x}I_x$.[53] Remarkably, $MAPbBr_{3-x}I_x/Pt$ exhibited a photocatalytic H_2 evolution rate of 651.2 $\mu mol\ h^{-1}$ (250 mg catalysts) under visible light (100 mW cm^{-2}, $\lambda \geq 420$ nm) and a solar-to-chemical conversion efficiency of 1.05%. Similarly, Wang et al. found that a high concentration of $MAPbBr_3$ can be stable in an aqueous solution of HBr, which can be split into H_2 and Br_2.[54] A high apparent quantum efficiency of $\approx 16.4\%$ for H_2 evolution at 420 nm was achieved over their modified photocatalyst (Pt/Ta_2O_5-$MAPbBr_3$-PEDOT:PSS). It should be reminded that the Pb-X (X = Cl, Br, I) are also photoactive materials, which may also contribute to the photocatalytic HI splitting reaction. Detailed and in-depth investigation may be needed to further reveal the effect of the Pb-X complex when using halide perovskite nanocrystals for photocatalysis.

2.3. In Non-Aqueous Reaction Solutions

Non-aqueous solution systems with a trace amount or in the absence of water are designed for CO_2 reduction reactions using halide perovskites. Ethyl acetate was selected by Su and co-workers for CO_2 reduction using $CsPbBr_3$ QDs/GO because of its mild polarity and high CO_2 solubility.[36] They reported that in ethyl acetate, $CsPbBr_3$ QDs catalyzed CO_2 reduction at an electron consumption rate of 23.7 $\mu mol\ g^{-1}\ h^{-1}$ with a selectivity of over 99.3% for CO_2 reduction rather than for proton reduction. After compositing with GO, the rate of electron consumption increased by 25.5% because of the improved electron extraction and transport. Analogous solution systems have also been adapted to other types of halide perovskites, such as $Cs_2AgBiBr_6$[55] and $CsPbBr_3$.[36,56] Ou et al. reported that acetonitrile with a trace amount of water (0.3 vol%) can also serve as a reaction solution for photocatalytic CO_2 reduction over halide perovskites.[57] The authors tested $CsPbBr_3$ QDs/g-C_3N_4 in acetonitrile/H_2O and achieved a 149 $\mu mol\ g^{-1}\ h^{-1}$ CO production rate from CO_2 under visible-light irradiation. Wu et al. recently carried out the same reaction in ethyl acetate solution with a higher water content of 1.2 vol%.[58] With CO_2 saturated in this medium, $MAPbI_3@PCN-221(Fe_x)$ exhibited a total yield of 1559 $\mu mol\ g^{-1}$ over an 80 h reaction period for CO (34%) and

**ADVANCED
SCIENCE NEWS**
www.advancedsciencenews.com

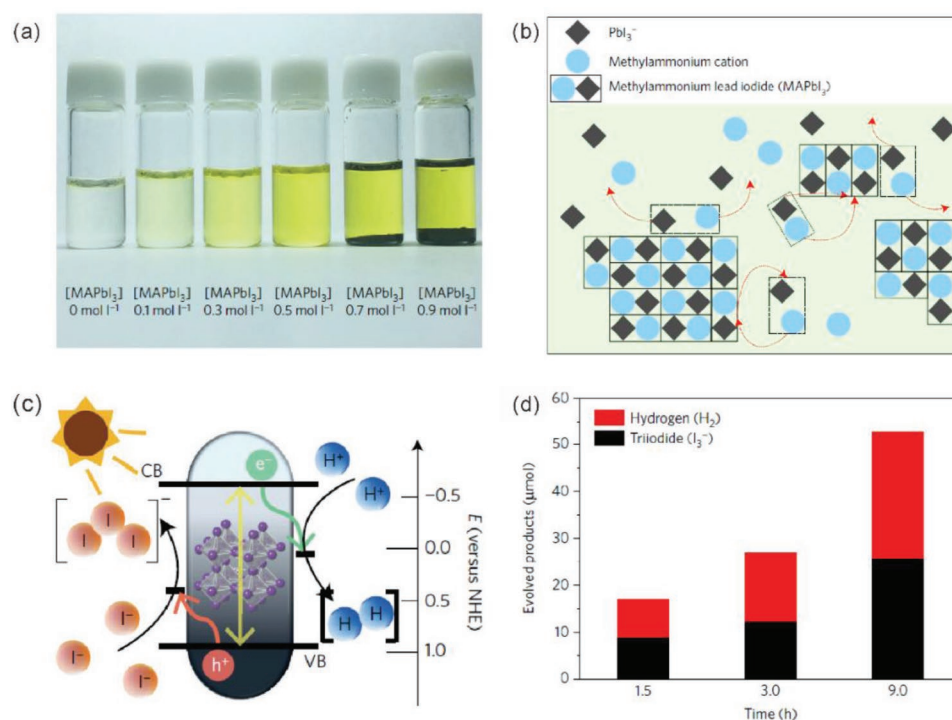**ADVANCED
ENERGY
MATERIALS**
www.advenergymat.de

Figure 4. a) $MAPbI_3$ in aqueous HI solution with different concentrations. b) Schematic illustration of $MAPbI_3$ powder in dynamic equilibrium with a saturated HI solution. Dotted lines represent the dissolution and precipitation of $MAPbI_3$ crystals and ions. c) Schematic band diagram of $MAPbI_3$ powder for the photocatalytic HI splitting reaction. d) Quantitative comparison between the amounts of H_2 and I_3^- evolved at different reaction times. Reproduced with permission.[50] Copyright 2016, Nature Publishing Group.

CH_4 (66%) production. Notably, this work quantificationally demonstrated that the oxidation product is O_2 that is originated from water oxidation rather than other products possibly from the oxidation of ethyl acetate in the CO_2-saturated ethyl acetate/water reaction solution.

The photocatalytic water or HI splitting and CO_2 reduction performance of halide perovskites is summarized in **Table 1**. The as-developed halide perovskite photocatalysts generally exhibit enough stability to withstand a photocatalytic test. However, the photocatalysts' efficiencies are still quite low, especially considering the remarkable photophysical properties halide perovskites possess. In addition, the conditions for the photocatalytic tests vary in different groups, thus making it difficult to fairly compare and evaluate the strategies researchers have applied to improve the efficiency. Therefore, we strongly suggest that the community follow standard test conditions and/or provide detailed experimental procedures for photocatalytic reactions. Moreover, it could be important to point out what are the other reaction products beside H_2 and the reduced CO_2 in a particulate photocatalysis system, because other reaction paths happened during photocatalysis could also contribute to producing the target product.[59]

3. Photoelectrode Thin-Film Systems

The first demonstration of a photoelectrode thin-film system, also known as a photoelectrochemical (PEC) cell, was by Fujishima and Honda in 1972 using a TiO_2 single-crystal wafer as the photoanode and Pt black as the cathode to split water under light irradiation and an applied bias.[40] A typical photoelectrochemical cell consists of a working electrode (i.e., photoelectrode), a counter electrode and a reference electrode (**Figure 5**). A photoelectrode can be fabricated by coating or growing several well-defined layers, such as a semiconductor layer, an electron/hole transport layer, and an electrocatalytic layer, onto a conductive substrate. Figure 5 shows a cell structure in which the working electrode functions as a photocathode. In the cell, electrons from the photoexcited semiconductor are generated at the electrode for reduction reactions, whereas holes are at the counter electrode for oxidation reactions.

The photoelectrode structure greatly relieves the harsh stability requirements for halide perovskites used in aqueous solutions, as it is technically much easier to coat a water-impermeable, conductive, and even catalytic layer onto the well-defined halide perovskite layer than onto the solution-phase nanocrystals. In practice, researchers indeed choose essentially the same strategy, coating layers onto a halide perovskite, to create stable halide perovskite photoelectrodes. To date, many types of such layers have been implemented, including a Ni layer (8 nm),[61] Field's metal (a fusible alloy that melts at $\approx$62 °C.),[37] Ti foil,[62] an In-Bi alloy layer[38] and a mesoporous carbon/graphite sheet.[63] In the following, we discuss these approaches by classifying them according to their target reactions, i.e., water oxidation, water reduction, and CO_2 reduction.

Table 1. Summary of the reported photocatalytic water or HI splitting and CO_2 reduction reactions using halide perovskites.

Materials	Reaction	Solution	Light source	Stability	Efficiency[a]	Ref.
$DMASnI_3$	H_2O red. to H_2	DI water	300-W Xe lamp (full spectrum)	>5 h	3.2 µmol g^{-1} h^{-1}	[43]
$MAPbI_3$	HI red. to H_2	Aqueous HI (with Pt)	Solar simulator (≥475 nm)	160 h	57 µmol g^{-1} h^{-1}; Solar to chemical (0.81%)	[50]
$MAPbI_3$/rGO	HI red. to H_2	Aqueous HI	120 mW cm^{-2} (≥420 nm)	200 h	939 µmol g^{-1} h^{-1}	[51]
$MAPbI_{3-x}Br_x$	HI red. to H_2	Aqueous HBr/HI (with Pt)	100 mW cm^{-2} (≥420 nm)	>30 h	2604 µmol g^{-1} h^{-1}; Solar to chemical (1.05%)	[52]
$CsPbI_{3-x}Br_x$	HBr red. to H_2	Aqueous HBr (with Pt)	120 mW cm^{-2} (≥420 nm)	>50 h	1120 µmol g^{-1} h^{-1}; AQE (2.5% @ 450 nm)	[53]
Pt/Ta_2O_5-$MAPbBr_3$-PEDOT: PSS	HBr red. to H_2	Aqueous HBr	150 mW cm^{-2} (≥420 nm)	>4 h	1050 µmol g^{-1} h^{-1}; AQE (16.4% @ 420 nm)	[54]
$CsPbBr_3$ QDs/GO	CO_2 red.	Ethyl acetate	150 mW cm^{-2} (AM 1.5G)	>12 h	29.8 µmol g^{-1} h^{-1}	[36]
$Cs_2AgBiBr_6$ NCs	CO_2 red.	Ethyl acetate	150 mW cm^{-2} (AM 1.5G)	>6 h	17.5 µmol g^{-1} h^{-1}	[55]
$CsPbBr_3$ QDs	CO_2 red.[b]	Ethyl acetate, H_2O (0.3 vol%)	AM 1.5G	>8 h	20.9 µmol g^{-1} h^{-1}	[56]
$CsPbBr_3$ QDs/g-C_3N_4	CO_2 red.	Acetonitrile, H_2O (0.3 vol%)	300-W Xe lamp (≥420 nm)	>6 h	149 µmol g^{-1} h^{-1} for CO production	[57]
$CsPbBr_3$@ZIF-67	CO_2 red.[b]	H_2O, CO_2 vapor	150 mW cm^{-2} (AM 1.5G)	>18 h	29.6 µmol g^{-1} h^{-1}	[46]
$CsPbBr_3$ QDs/UiO-66(NH_2)	CO_2 red.	Ethyl acetate, H_2O (0.3 vol%)	300-W Xe lamp (≥420 nm)	>12 h	8.2 µmol g^{-1} h^{-1} for CO production	[60]
$MAPbI_3$@PCN-221(Fe_x)	CO_2 red.[c]	Ethyl acetate, H_2O (1.2 vol%)	300-W Xe lamp (≥400 nm)	80 h	19.5 µmol g^{-1} h^{-1}	[58]

[a]For proton reduction, values pertain to the H_2 production rate; for CO_2 reduction, values pertain to the electron consumption rate unless otherwise noted. The rates were converted to µmol g^{-1} h^{-1}; [b]Oxygen was measured in these works but not quantified; [c]Oxygen generated was measured and quantified.

3.1. Water Oxidation

Metal-based materials were first used to protect halide perovskite photoelectrodes. In 2015, Da et al. reported the first multi-layered $MAPbI_3$-based photoanode with an ultrathin Ni surface layer (8 nm) deposited by magnetron sputtering. The Ni layer functioned as both a physical passivation barrier and a hole-transferring catalyst for water oxidation (**Figure 6**a).[61] Note that the surface of Ni was gradually converted to nickel oxide. The photoanode exhibited a photocurrent density of over 10 mA cm^{-2} in 0.1 M Na_2S at 0 V versus Ag/AgCl under AM 1.5G simulated sunlight at 100 mW cm^{-2}. However, the photocurrent of

the photoanode could be maintained above 2 mA cm^{-2} for only 15–20 min. Wang et al. applied this ultrathin Ni passivation strategy to their surface-functionalized $MAPbI_3$ and further improved the stability to ≈30 min, but the photocurrent density was reduced to 2.1 mA cm^{-2}.[64] Building on this layered structure with Ni as the protective and catalytic layer, in 2016, Hoang et al. further used a dense hole-transport layer to enhance the stability of the $MAPbI_3$ photoelectrode.[65] The device stability was increased from 15 min to more than 30 min. Later in 2018, Nam et al. have fabricated a more stable $MAPbI_3$ photoanode by introducing a low-melting-point Field's metal layer between the perovskite and Ni layers.[66] The perovskite photoanode was found to be stable for 6 h at ≈13 mA cm^{-2} under 0.7 Sun illumination and a bias of 1.3 V versus reversible hydrogen electrode (RHE) in potassium hydroxide solution (KOH) solution.

Carbon materials have also been employed as protective layers for halide perovskites. Tao et al. encapsulated a $(5\text{-}AVA)_x(MA)_{1-x}PbI_3$ [5-AVA = $HOOC(CH_2)_4NH_3^+$]-based photoanode with conductive carbon paste and silver conductive paint for water oxidation.[67] The photoanode achieved unprecedented stability, remaining stable in an alkaline electrolyte for more than 48 h. The material also showed a high photocurrent density of 12.4 mA cm^{-2} at 1.23 V versus RHE in an alkaline electrolyte. This high stability was largely due to the coating of a thick carbon layer (several hundreds of micrometers) onto the halide perovskites. Very recently, Poli et al. used a commercial thermal graphite sheet and a mesoporous carbon scaffold to encapsulate a $CsPbBr_3$-based photoanode (Figure 6b).[63] A record stability of 30 h in aqueous electrolyte with current above 2 mA cm^{-2} at 1.23 versus RHE was achieved under constant simulated solar illumination. Furthermore, by functionalizing the surface of the graphite sheet with an Ir-based
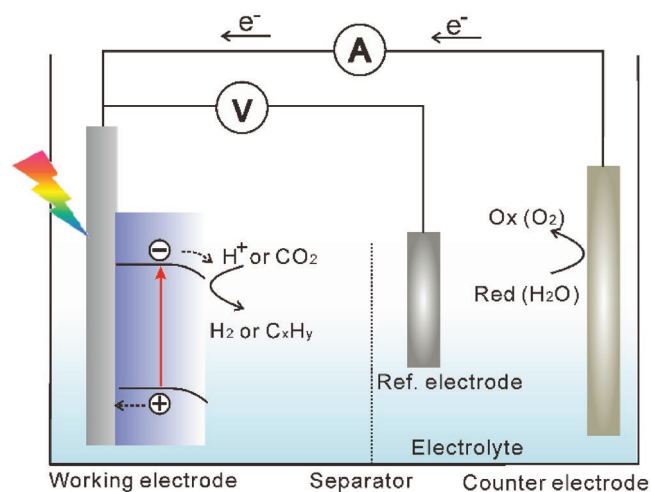

Figure 5. An illustration of a three-electrode photoelectrochemical (PEC) cell. The working electrode functions as a photocathode.

**ADVANCED
SCIENCE NEWS**

www.advancedsciencenews.com
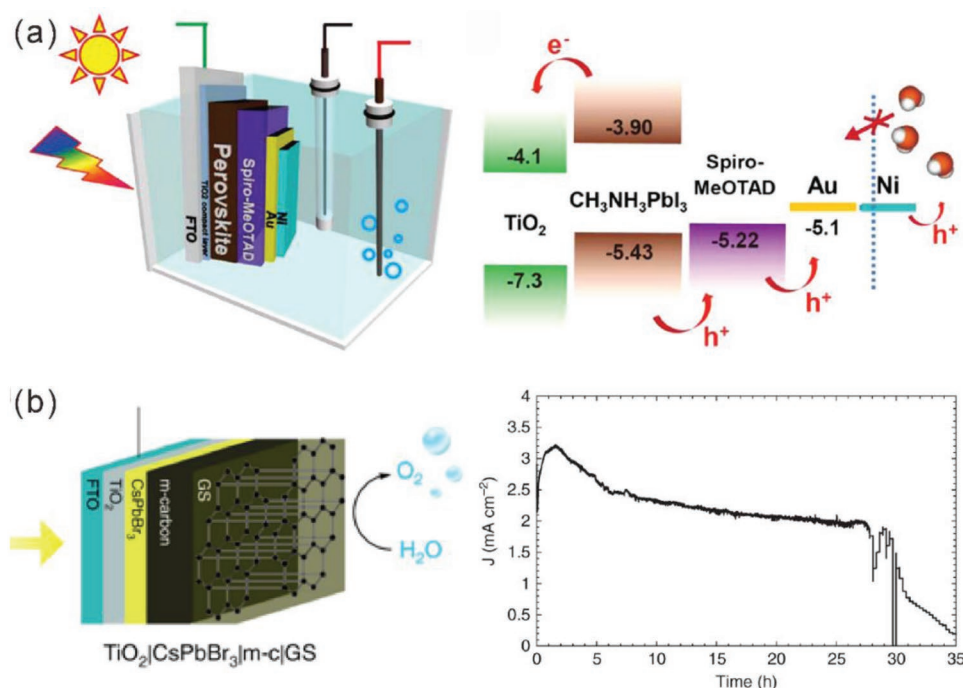
**ADVANCED
ENERGY
MATERIALS**

www.advenergymat.de

Figure 6. a) Schematic illustration of photoelectrochemical test of a Ni-coated perovskite photoanode in a standard three-electrode system. The panel on the right shows the schematic energy diagram of the photoelectrode. Reproduced with permission.[61] Copyright 2015, American Chemical Society. b) Schematic illustration of the $CsPbBr_3$ photoanode for O_2 evolution. The panel on the right shows the current density as a measure of the stability of the photoanode in water. Reproduced with permission.[63] Copyright 2019, Nature Publishing Group.

water oxidation catalyst (WOC), the onset potential of the composite photoanode was cathodically shifted by 100 mV. Notably, ≈9 μmol of evolved O_2 were detected over a ≈130 min test using their TiO_2 | $CsPbBr_3$ | m-c | GS | WOC photoelectrode under continuous simulated solar light irradiation (AM 1.5G, 100 mW cm^{-2}) in 0.1 M KNO_3 adjusted to pH 3.5 with H_2SO_4. This achievement marks by far the most stable and efficient halide perovskite photoanode for water oxidation.
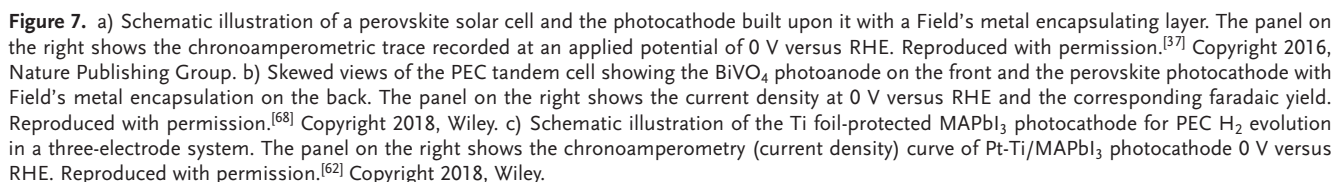
3.2. Water Reduction

Field's metal is the most widely used protective and conductive layer since its first demonstration by the Reisner group as a coating onto a $MAPbI_3$-based photocathode for water reduction (**Figure 7**a).[37] With Pt nanoparticles loaded as the hydrogen evolution electrocatalysts, the Reisner group obtained a record photocurrent density of 9.8 mA cm^{-2} at 0 V versus RHE with an onset potential of 0.95 ± 0.03 versus RHE. The photoelectrode showed high stability, retaining more than 80% of its initial photocurrent for ≈1 h under continuous illumination (100 mW cm^{-2}, AM 1.5G, λ > 400 nm). The group further fabricated a tandem PEC system by coupling a Field's metal-protected cesium formamidinium methylammonium (CsFAMA) triple cation mixed halide perovskite photocathode with a stable $BiVO_4$|TiCo photoanode for bias-free solar-to-hydrogen (STH) production (Figure 7b).[68] The perovskite photocathode alone could operate for up to 7 h with a photocurrent density of 12.1 ± 0.3 mA cm^{-2} at 0 V versus RHE. After coupling with a $BiVO_4$ photoanode, the PEC tandem system, with a device

surface area of 0.25 cm^2, could operate for up to 20 h with a bias-free STH efficiency of 0.35 ± 0.14%. Remarkably, because the fabrication method is highly reproducible, the tandem device could be scaled up to 10 cm^2 with only a slight drop in the photocurrent density. Also using Field's metal as the protective layer, Gao et al. fabricated an all-inorganic photocathode by incorporating $CsPbBr_3$ as the perovskite layer and NiO and ZnO as the hole and electron transport layers, respectively.[69] This all-inorganic photocathode achieved a photocurrent of ≈1.2 mA cm^{-2} at 0 V versus RHE and retained ≈94% of its initial photocurrent after continuous illumination for 1 h (AM 1.5G).

Titanium foil is another good choice for protecting halide perovskite photoelectrodes. Zhang et al. fabricated a sandwich-like structure by pasting Ti foil onto a $MAPbI_3$-based photocathode (Figure 7c).[62] With Pt loaded as the catalyst, this photocathode exhibited an onset potential at 0.95 V versus RHE and a photocurrent density of 18 mA cm^{-2} at 0 V versus RHE, with an ideal ratiometric power-saved efficiency of 7.63%. Impressively, the photocathode retained good stability under 12 h of continuous illumination in water over a wide pH range.

3.3. CO$_2$ Reduction

One aim of CO_2 reduction is to alleviate the energy crisis and environmental issues by producing C_1–C_3 chemical fuels. The products of photoelectrocatalytic CO_2 reduction in aqueous media can be mixtures of formic acid, carbon

Figure 7. a) Schematic illustration of a perovskite solar cell and the photocathode built upon it with a Field's metal encapsulating layer. The panel on the right shows the chronoamperometric trace recorded at an applied potential of 0 V versus RHE. Reproduced with permission.[37] Copyright 2016, Nature Publishing Group. b) Skewed views of the PEC tandem cell showing the $BiVO_4$ photoanode on the front and the perovskite photocathode with Field's metal encapsulation on the back. The panel on the right shows the current density at 0 V versus RHE and the corresponding faradaic yield. Reproduced with permission.[68] Copyright 2018, Wiley. c) Schematic illustration of the Ti foil-protected $MAPbI_3$ photocathode for PEC H_2 evolution in a three-electrode system. The panel on the right shows the chronoamperometry (current density) curve of $Pt-Ti/MAPbI_3$ photocathode 0 V versus RHE. Reproduced with permission.[62] Copyright 2018, Wiley.

monoxide, formaldehyde, methane, and C_2–C_3 hydrocarbons. In this context, the goal of CO_2 reduction is to efficiently, stably, and selectively produce a target product. Thermodynamically, halide perovskites can drive CO_2 reduction reactions because they generally possess sufficiently negative conduction band potentials (Figure 1). However, CO_2 reduction using a halide perovskite-based photoelectrode has scarcely been reported. Encouragingly, Chen et al. recently demonstrated In-Bi alloy-coated $MAPbI_3$-based photocathodes for selective CO_2 reduction with nearly 100% faradaic efficiency (FE) for formic acid production in aqueous solution (**Figure 8**a).[38] The $In_{0.4}Bi_{0.6}$ composition was identified by a compositional screening strategy of a ternary In-Bi-Sn low melting-point alloy system. The photocathode was then fabricated by coating the catalytic, protective, and conductive $In_{0.4}Bi_{0.6}$ alloy layer onto the halide perovskite. The photocathode operated at –0.6 V versus RHE under simulated AM 1.5G irradiation for more than 1.5 h (Figure 8b) and achieved a photo-assisted electrolysis system efficiency of 7.2%.

Studies detailing the use of halide perovskite-based photoelectrodes for water splitting and CO_2 reduction are summarized in **Table 2**. As indicated, the as-developed halide perovskite photoelectrodes generally exhibit better stability than the photocatalysts, because the well-defined perovskite layers are well protected in the photoelectrodes. The overall performance (including stability and efficiency) of the photoelectrodes is quite promising, with the $CsPbBr_3$|mesoporous carbon|graphite sheet|Ir OER and $(CsMAFA)PbI_xBr_{3-x}$|FM|Pt–$BiVO_4$|TiCo designs considered the best for water oxidation and reduction, respectively. However, the photoelectrodes for CO_2 reduction have been rarely reported. Moreover, many works only demonstrated the photocurrent, which might not be a good criterion for evaluating the efficiency because the photocurrent can also originate from the corrosion of the electrodes or other side reactions. It is thus encouraged that the researchers report the solar to product conversion efficiency as well as the products in the future if possible. We believe that there is much more to be done regarding water splitting and selective CO_2 reduction to a target chemical fuel using halide perovskite photoelectrodes.

**ADVANCED
SCIENCE NEWS**

www.advancedsciencenews.com

**ADVANCED
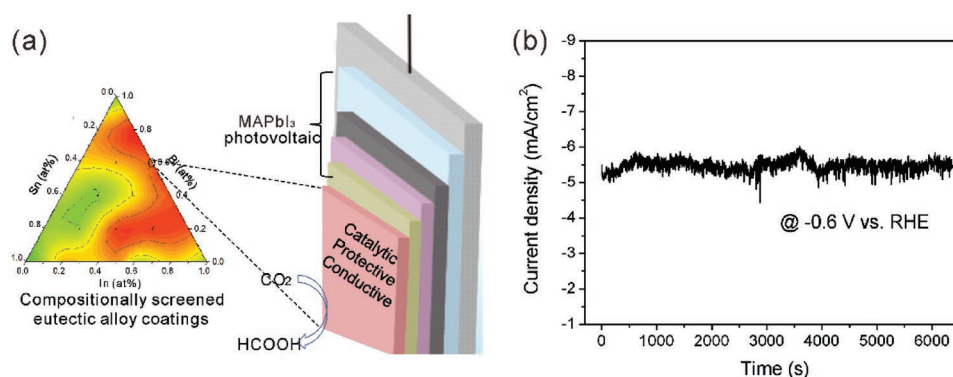ENERGY
MATERIALS**

www.advenergymat.de

Figure 8. a) Schematic illustration of the compositional screening and photoelectrode structure of the catalytic alloy protected MAPbI$_3$ photocathode. b) Stability of the photocathode under irradiation at −0.6 V versus RHE under AM 1.5G irradiation. Reproduced with permission.[38] Copyright 2019, American Chemical Society.

4. Perovskite Photovoltaics Integrated with (Photo)Electrocatalysis

Halide perovskite PVs can be aligned with a photoelectrode for wide-spectrum solar-to-chemical fuel conversion or can act as an external circuit to power an electrocatalytic cell. A simplified illustration of a PV-integrated (photo)electrocatalytic system is shown in **Figure 9**, in which the PV absorbs light and provides the needed photovoltage for the both cathodic and anodic reactions to occur.

Table 2. A summary of the reported photoelectrodes using halide perovskites. FM: Field's metal; FE: faradaic efficiency; STH: solar-to-hydrogen efficiency.

Photoelectrode	Reaction	Electrolyte	Light source	Stability	Efficiency	Ref.
MAPbI$_3$|Ni	H$_2$O Ox	0.1 M Na$_2$S	100 mW cm^{-2}, AM 1.5G	15–20 min	10 mA cm^{-2} @ 0 V vs Ag/AgCl	[61]
Surface-functionalized MAPbI$_3$|Ni	H$_2$O Ox	0.1 M Na$_2$S	100 mW cm^{-2}, AM 1.5G	>30 min	2.1 mA cm^{-2} @ 0 V vs Ag/AgCl	[64]
MAPbI$_3$|pinhole-free HTL|Ni	H$_2$O Ox	Not clear	Simulated illumination (0.7 Sun)	>30 min	17.4 mA cm^{-2} @ 1.23 V vs SHE	[65]
MAPbI$_3$|FM|Ni	H$_2$O Ox	1.0 M KOH solution	Simulated illumination (0.7 Sun)	6 h	13 mA cm^{-2} @ 1.3 V vs RHE	[66]
(5-AVA)$_x$(MA)$_{1-x}$PbI$_3$|conductive carbon paste	H$_2$O Ox[a]	1.0 M KOH solution	100 mW cm^{-2}, AM 1.5G	>48 h	12.4 mA cm^{-2} @ 1.23 V vs RHE	[67]
CsPbBr$_3$|mesoporous carbon|graphite sheet|Ir OER	H$_2$O Ox[a]	0.1 M KNO$_3$	100 mW cm^{-2}, AM 1.5G	30 h	2 mA cm^{-2} @ 1.23 V vs RHE	[63]
MAPbI$_3$|FM|Pt	H$_2$O red.	0.1 M borate	100 mW cm^{-2}, AM 1.5G, λ > 400 nm	>1 h	9.8 mA cm^{-2} @ 0 V vs RHE; FE ≈ 95%	[37]
(CsMAFA)PbI$_x$Br$_{3-x}$|FM|Pt–BiVO$_4$|TiCo (0.25 cm^2)	H$_2$O red.	0.1 M borate, K$_2$SO$_4$	100 mW cm^{-2}, AM 1.5G	18 h	≈0.39 mA cm^{-2} (no-bias); STH ≈ 0.35%	[68]
(CsMAFA)PbI$_x$Br$_{3-x}$|FM|Pt–BiVO$_4$|TiCo (10 cm^2)	H$_2$O red.	0.1 M borate, K$_2$SO$_4$	100 mW cm^{-2}, AM 1.5G	14 h	≈0.23 mA cm^{-2} (no-bias); STH ≈ 0.15%	[68]
CsPbBr$_3$|FM|Pt	H$_2$O red.	0.2 M Na$_2$HPO$_4$/ NaH$_2$PO$_4$	100 mW cm^{-2}, AM 1.5G	>1 h	1.2 mA cm^{-2} @ 0 V vs RHE	[69]
MAPbI$_3$|Ti foil|Pt	H$_2$O red.	0.5 M H$_2$SO$_4$	100 mW cm^{-2}, AM 1.5G	12 h	18 mA cm^{-2} @ 0 V vs RHE. Ideal ratiometric power-saved efficiency of 7.63%	[62]
CsFAMA perovskite|Al-ZnO|FM|Pt	H$_2$O red.	0.1 M potassium phosphate	100 mW cm^{-2}, AM 1.5G	18 h	14.3 mA cm^{-2} @ 0 V vs RHE FE(H$_2$) of ≈72%	[70]
CsFAMA perovskite|PCBM+ALD TiO$_2$|Pt	H$_2$O red.	0.5 M H$_2$SO$_4$	0.5 Sun	2 h in acid (75% photocurrent left)	>10 mA cm^{-2} @ 0 V vs RHE	[71]
MAPbI$_3$|In$_{0.4}$Bi$_{0.6}$	CO$_2$ red.	0.1 M KHCO$_3$	100 mW cm^{-2}, AM 1.5G	>1.5 h	≈5.2 mA cm^{-2} @ −0.6 V vs RHE. photo-assisted electrocatalysis efficiency of 7.2%	[38]

[a]Oxygen was measured and quantified in these works.

**ADVANCED
SCIENCE NEWS**
www.advancedsciencenews.com
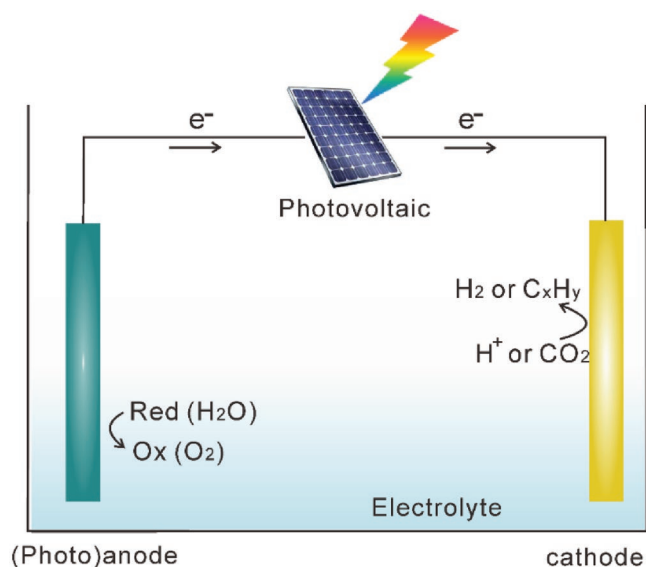
**ADVANCED
ENERGY
MATERIALS**
www.advenergymat.de

Figure 9. An illustration of a photovoltaic-integrated (photo)electrocatalysis system. The anode can also be photoactive in this case.

In a PV–PEC (where the electrodes are photoactive) or PV–EC system, the halide perovskite PV is isolated from the solution, acting as the photovoltaic power source for an unbiased solar-to-chemical fuel conversion device. In such devices, the halide perovskite-based photovoltaics can provide all the voltage needed to drive a water splitting or CO_2 reduction reaction without the help of an external power source. Halide perovskite PVs generally have large open-circuit voltages (1–1.4 eV). Therefore, two halide perovskite PV cells in tandem are enough to drive overall water splitting, whereas three cells in tandem are needed when using conventional Si and CIGS PVs. In addition, the cost of solution-processable halide perovskite PVs is much lower than that of Si or CIGS cells. In the following, we discuss the progress made in the development of PV-(photo)electrocatalysis systems.

4.1. Photovoltaic Integrated with Photoelectrocatalysis

In an integrated PV–PEC system, a photoanode or photocathode is connected in series to a halide perovskite PV. The photoanode(cathode) is often stacked on top of the halide perovskite PV because of its larger bandgap (>2 eV) than that of the halide perovskite. $BiVO_4$ is the most well-studied photoanode for water oxidation due to its suitable bandgap (2.4 eV) and superior PEC performance. In 2015, Kamat group demonstrated an all-solution-processed tandem water-splitting device composed of a cobalt phosphate (CoPi) catalyst-modified $BiVO_4$ photoanode and a single-junction $MAPbI_3$ perovskite solar cell.[72] As shown in **Figure 10**a, the perovskite solar cell is placed under the $BiVO_4$ photoanode so that wavelengths >500 nm can pass through the $BiVO_4$ photoanode. To make full use of the lower-energy light in the bottom layer, the top layer should be highly transparent (Figure 10b, with $BiVO_4$ as the top layer). Because two modules are connected in series, the operating photocurrent density of a tandem PV-photoanode

device can be predicted from the intersection of the individual J–V curves (Figure 10c). This PV-photoanode device exhibited an STH efficiency of 2.5% at neutral pH without external bias (Figure 10d). Kim et al. applied a dual-doping strategy (hydrogen treatment and 3 at% Mo doping) to modify the $BiVO_4$ photoanode and then loaded cobalt carbonate (Co–Ci) as a catalyst. They further fabricated a $MAPbI_3$ PV–$BiVO_4$ photoanode tandem device with an STH efficiency of 4.3% in the wired configuration and 3.0% in the wireless configuration for a long stability test (12 h).[73] Fe_2O_3 is another widely studied photoanode for halide perovskite PV–PEC tandem devices. Gurudayal et al. demonstrated that a $MAPbI_3$ solar cell in tandem with a Fe_2O_3 photoanode can achieve overall water splitting with an STH efficiency of 2.4%.[74] Other photoanodes such as TiO_2, CdS, $BiVO_4/WO_3$, and $BiVO_4/WO_3/SnO_2$ have also been integrated with halide perovskite solar cells, as summarized in **Table 3**. In addition to photoanodes, photocathodes have also been used in tandem devices with halide perovskite PVs. Mayer group fabricated a tandem device using a Cu_2O as the photocathode and a $FA_xMA_{1-x}PbI_3$ solar cell connected to an IrO_2 as the anode.[75] This device yield an STH of 2.5% for unbiased water splitting.

As summarized in Table 3, most halide perovskite solar cells incorporated into PV–PEC tandem devices are based on $MAPbI_3$ because of the material's relatively small bandgap (≈1.55 eV). However, one of the most important advantages of halide perovskites is their bandgap tunability (1.1–2.3 eV), which can lead to compatibility with a wide variety of photoelectrodes. Recently, cation (Cs^+, FA^+ and MA^+) and anion (Br^- and I^-) mixed halide perovskites have been demonstrated to have large open-circuit voltages and good stability, resulting in excellent tandem device performance when integrated with a Mo:$BiVO_4$ photoanode.[76] In addition, Luo et al. fabricated a large-bandgap perovskite $MAPbBr_3$ (E_g = 2.3 eV) PV-photocathode tandem device, in which the photocathode was made of small-bandgap $CuIn_xGa_{1-x}Se_2$ (1.1 eV).[77] Therefore, the halide perovskite solar cell was stacked on top of the photocathode. This tandem device yielded a high STH of ≈6%.

One of the key requirements of a PV–PEC tandem device is that the top layer with larger bandgap should be highly transparent. One way to meet this requirement when using an opaque photoanode(cathode) is to use a beam splitter to separate the solar spectrum into two light beams, which will be irradiated onto the photoanode(cathode) and solar cell separately.[76,78] Another key issue is the significant energy loss due to the mismatch between the photocurrent of the wide-bandgap photoanode(cathode) and that of the narrow-bandgap solar cell (Figure 10c). Therefore, further improving the current of the photoanode(cathode) to make it compatible with that of the solar cell is crucial for improving the STH efficiency. To this end, the Sharp group has demonstrated a new three-terminal cell design in which a second junction is added to extract charge carriers that cannot be injected into the top junction due to current mismatch.[79] This concept may be applied to halide perovskite PV–PEC tandem devices in the future.

Unlike the vastly reported study of water splitting, the study of CO_2 reduction using a PV–PEC tandem device is so far rarely reported. Jang et al. reported CO_2-to-CO conversion using a $MAPbI_3$ PV-ZnO@ZnTe@CdTe core–shell nanorod
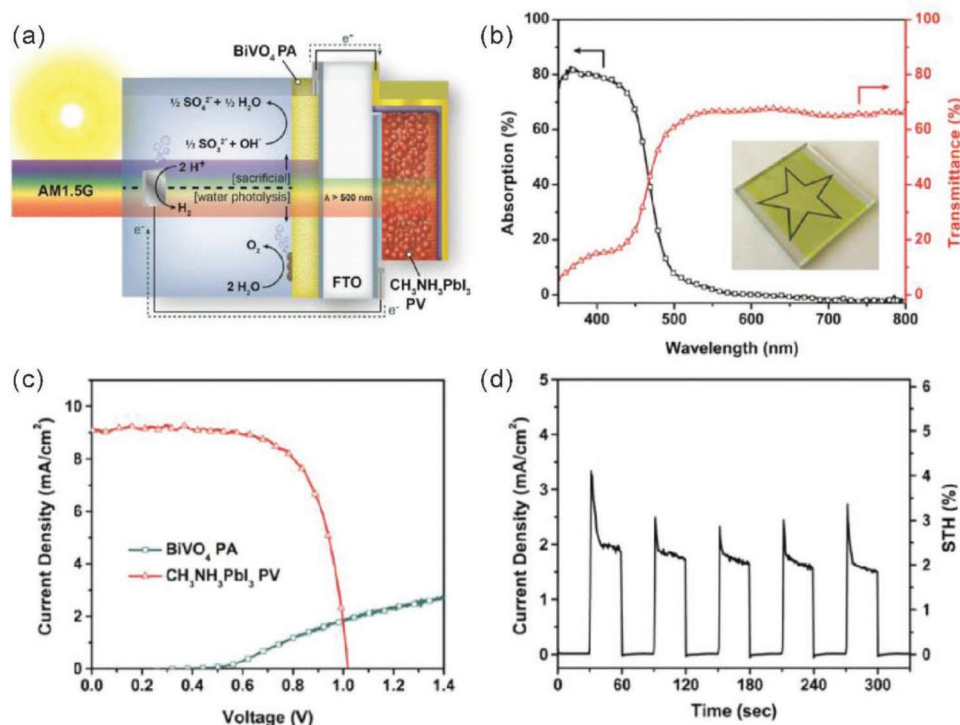
Figure 10. a) Schematic diagram of a tandem MAPbI$_3$ PV–BiVO$_4$ device for solar-to-chemical fuel generation. b) Optical absorption and transmittance of the BiVO$_4$ thin film. Inset: photograph demonstrating the translucence and limited visible-light scattering of the spin-cast BiVO$_4$ thin film. c) Overlaid $J–V$ characteristics of CoPi/BiVO$_4$ photoanode and MAPbI$_3$ solar cell. The photovoltaic parameters were recorded through a CoPi/BiVO$_4$ film. CoPi/BiVO$_4$ was measured in a three-electrode configuration with an Ag/AgCl reference electrode and a Pt counter electrode. The crossing point of the two curves designates the anticipated photocurrent output of the series-connected tandem device. d) Photocurrent density and calculated STH efficiency as a function of time for the MAPbI$_3$-CoPi/BiVO$_4$ device, demonstrating the ability to drive neutral water oxidation and reduction at 2.5% efficiency without external bias. Reproduced with permission.[72] Copyright 2015, American Chemical Society.

Table 3. Summary of reported halide perovskites photovoltaics integrated with photoelectrocatalysis systems for water splitting. STH: solar-to-hydrogen conversion efficiency. BVO: BiVO$_4$.

Photovoltaic	Photoanode	Area [cm^2]	Electrolyte	Stability	STH	Ref.
MAPbI$_3$	TiO$_2$@BVO	/	0.1 M PBS	0.8 h	1.24%[a]	[81]
MAPbI$_3$	CoPi/BVO	0.54	0.1 M KPi	5 min	2.5%	[72]
MAPbI$_3$	Co–Ci/Mo:BVO	0.45	0.1 M KCl	12 h	4.3% (wired); 3% (wireless)[a]	[73]
MAPbI$_3$	CoPi/Mn:Fe$_2$O$_3$	0.12	1 M NaOH	8 h	2.4%[a]	[74]
MAPbI$_3$	Sn:TiO$_2$	0.13	1 M KOH	2 h	1.5%	[82]
MAPbI$_3$	NiOOH/FeOOH/BVO/WO$_3$	0.5	0.5 M KPi	1 h	≈3.3%	[83]
MAPbI$_3$	CoPi/Sn:Fe$_2$O$_3$	0.12	1 M NaOH	120 s	3.4%	[84]
MAPbI$_3$	CoO$_x$/BVO/WO$_3$/SnO$_2$	0.196	0.5 M KPi	15 min	4.5%[a]	[85]
Cs$_{0.05}$(FA$_{0.83}$MA$_{0.17}$)$_{0.95}$Pb(I$_{0.83}$Br$_{0.17}$)$_3$	NiOOH/FeOOH/BVO	/	1 M KBi	10 h	6.5%[a]	[86]
MAPbI$_3$	CdS/TiO$_2$	1	0.1 M NaOH	1 h	1.54%	[87]
MAPbI$_3$	NiOOH/FeOOH/Mo: BVO	0.25	0.5 M KPi	10 h	6.2%[a]	[78]
FA$_{0.83}$Cs$_{0.17}$PbI$_2$Br	NiOOH/FeOOH/Mo: BVO	0.25	0.5 M KPi	6 h	6.3%[a]	[76]
CIGS (photocathode)	MAPbBr$_3$/DSA	0.16	0.5 M H$_2$SO$_4$	180 s	6%	[77]
Cu$_2$O (photocathode)	FA$_x$MA$_{1-x}$PbI$_3$/IrO$_2$	0.057	0.5 M Na$_2$SO$_4$, 0.1 M NaPi	2 h	2.5%[a]	[75]

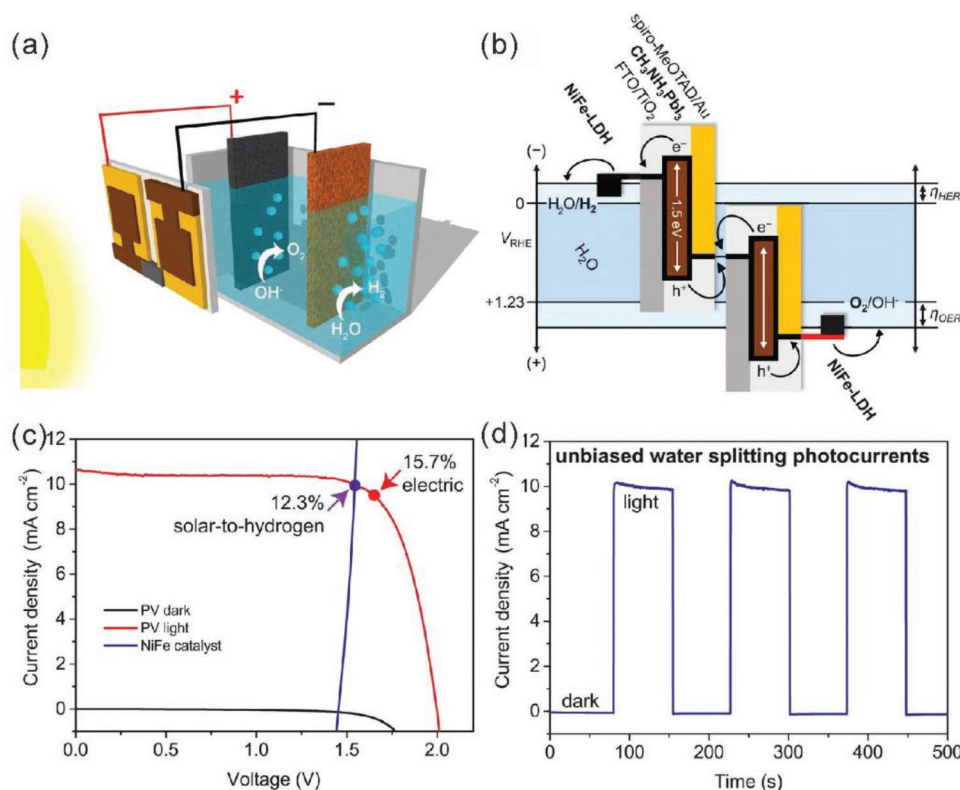[a]Oxygen was measured and quantified in these works.

Figure 11. a) Schematic diagram of a water-splitting device. b) A generalized energy schematic of the perovskite tandem cell for water splitting. c) $J–V$ curves of the perovskite tandem cell in the dark and under simulated illumination (100 mW cm^{-2}, AM 1.5G) and of the NiFe layered double hydroxides (LDH) electrodes in a two-electrode configuration. d) Current density-time profile of the integrated water-splitting device without external bias under a chopped simulated illumination (100 mW cm^{-2}, AM 1.5G). Reproduced with permission.[8] Copyright 2014, AAAS.

array photocathode in tandem.[80] With solar energy as the only energy source, this tandem device achieved a solar-to-CO conversion efficiency of 0.35%.

4.2. Photovoltaics Integrated with Electrocatalysis

Perovskite solar cells can serve as separate and external power sources to generate sufficient voltages to drive electrocatalysis. Grätzel and co-workers were first to demonstrate that two perovskite solar cells in tandem could power overall water splitting (**Figure 11**).[8] Specifically, they used a MAPbI$_3$-based solar cell with a short-circuit photocurrent density (J_{sc}), open-circuit voltage (V_{oc}), fill factor and PCE of 21.3 mA cm^{-2}, 1.06 V, 0.76% and 17.3%, respectively. The electrocatalysts for both water reduction and oxidation were earth-abundant and robust NiFe layered double hydroxides (LDHs), which only required 1.7 V across the electrodes to achieve a 10 mA cm^{-2} water-splitting current in a 1 M NaOH aqueous electrolyte. Then, an overall water-splitting cell was assembled by connecting two MAPbI$_3$ solar cells (a tandem cell) to the NiFe LDH electrodes (Figure 11a,b). The tandem cell exhibited a $J–V$ response with a V_{oc} of 2.00 V and a PCE of 15.7%, as depicted in Figure 11c. The authors predicted the operating current density of the integrated system (normalized to the total illuminated area of the solar cells) by defining the intersection of the $J–V$ curves of the tandem cell and the catalyst electrodes in the two-electrode configuration as the operating point. At this point, an operating current density of 10 mA cm^{-2} and STH of 12.3% can be obtained. This operating point of the water-splitting cell occurs very close to the maximum power point of the perovskite tandem cell (9.61 mA cm^{-2} at 1.63 V, PCE 15.7%), indicating that minimal energy is lost in converting electrical to chemical energy in this system. The authors further measured the current density in the standalone, unbiased light-driven configuration to confirm that the system indeed operated at 10 mA cm^{-2} with an STH of 12.3% (Figure 11d).

One of the drawbacks of this PV-electrocatalysis design is that the electrocatalyst for both water oxidation and water reduction in the same solution is very limited. In this regard, Grätzel and co-workers modified their electrocatalytic cell by separating the anode half-cell and cathode half-cell using a bipolar membrane.[88] With this approach, the authors were able to expand the selection of a H$_2$ evolution catalyst in acid solution and an O$_2$ evolution catalyst in alkaline solution. Specifically, the authors selected CoP as the H$_2$ evolution catalyst in 0.5 M H$_2$SO$_4$ and NiFe LDH as the O$_2$ evolution catalyst in 1 M KOH. This cell only required 1.63 V to achieve a photocurrent density of 10 mA cm^{-2}. Thus, a high STH conversion efficiency of 12.7% was achieved upon the integration of the perovskite PV cell with this newly designed electrocatalytic cell.

The Grätzel group also applied this integrated PV–EC structure to reduce CO$_2$ to CO.[89] Three MAPbI$_3$ solar cells were

connected in tandem to serve as a power source with a V_{oc} of 3.1 V, J_{sc} of 6.15 mA cm^{-2} and PCE of 13.4%. Au and IrO$_2$ were selected as the electrocatalysts for CO$_2$ reduction and water oxidation at the cathode and anode ends, respectively. Powering this Au-IrO$_2$ electrocatalytic cell requires a driving voltage of at least 2 V, considering the thermodynamic voltage (CO$_2$ ⇌ CO + 1/2O$_2$; $\Delta E = 1.34$ V) and the overpotentials for the two electrodes (0.3 V on the cathode Au, 0.4 V on the anode IrO$_2$). The perovskite tandem cell was then integrated with the electrocatalytic cell to form a PV-electrocatalysis cell, operated at 5.8 mA cm^{-2} for at least 18 h with a solar-to-CO efficiency exceeding 6.5%. This work represents a benchmark in sunlight-driven CO$_2$ conversion.

5. Conclusion and Future Prospects

While considerable effort has been devoted to studying different aspects of solar-to-chemical fuel conversions, the slow reaction rates, lack of efficient and stable materials, and the low energy density of sun light on the earth's surface (1 kW m^{-2}), have hindered the development of solar-to-chemical fuel conversion approaches. Moreover, the complexity of the multicomponent photocatalysts and devices, and the nature of reaction media (aqueous environment) limit in-depth and/or in situ investigations of the materials using diffraction and electron spectroscopy-based techniques.

The recently discovered remarkable photophysical properties of halide perovskite semiconductors give hope for achieving practical solar-to-chemical fuel conversion approaches by utilizing those semiconductors. To date, various halide perovskite photocatalysts, photoelectrodes and reaction system configurations have been designed, studied, tested, and further improved. For instance, H$_2$ can be produced from HI using MAPbI$_3$ photocatalysts; photocatalytic CO$_2$ reduction can be achieved in ethyl acetate with CsPbBr$_3$ photocatalysts; and MAPbI$_3$ can be used as a photocathode or photoanode for reduction and oxidation reactions, respectively. Moreover, halide perovskite-based photovoltaics can be integrated with photoelectrocatalytic or electrocatalytic cells for bias-free water splitting or CO$_2$ reduction. Nevertheless, despite the efforts and achievements summarized above, halide perovskite materials are still in the early stages of exploration for solar-to-chemical fuel conversion systems. There is much room to enhance their stability, efficiency, and environmental friendliness for future practical applications. Below we mention several possible directions and associated challenges that are worthy of investigation in this area.

1) Functional perovskite@shell core–shell structures need to be further explored. A semiconducting or conducting shell will likely be needed to encapsulate a perovskite-core nanostructure for use in aqueous media. The shells could further facilitate charge carrier transfer via interfacial or band-alignment engineering across the core–shell structures. Functionalization of the shells with nanoparticles or ligands will enhance the efficiency of solar-to-chemical fuel conversion and enable a wide scope of photocatalytic applications (for example organic reactions[90–92]) beyond water splitting and CO$_2$ reduction. However, construction of perovskite@shell structures remains challenging, largely because halide perovskite materials are incompatible with the polar solvents that are typically used for shell formation reactions.

2) New protective layers or ligands should be developed for halide perovskites by exploring various coating and growth methodologies. Beyond merely the selection of new materials, coating halide perovskite photoelectrodes, or photovoltaics with a functional layer will require in-depth understanding of deposition approaches and their effect on the perovskite material. At present, most of the attention is paid to solution-based and evaporative growth methods for layers, while not enough attention is paid to hybrid, combination approaches and solid-to-melt approaches for coating design. Moreover, designing of the ligands that stabilized halide perovskite nanocrystals to be electron-donating or electron-withdrawing may also contribute to the reduction or oxidation reactions.

3) Additional attention should be directed to halide perovskite nanostructures. The effect of surface reactivity on the catalytic properties and phase stability of halide perovskite nanostructures becomes significant because of their large surface-area-to-volume ratios. Nanostructure design could fundamentally help in understanding structure-sensitive properties and the dynamics between surface and bulk, which will promote the discovery of active and stable catalysts with enriched surface-active sites.

4) The design of reaction solution systems and tandem device configurations need further optimization. Reaction systems of various viable solutions should be explored for halide perovskites in conjunction with targeting reactions beyond water splitting or CO$_2$ reduction. As for tandem device configurations, issues such as electrical current mismatch, opaque top layers, and large series resistance need to be solved.

5) Attention should be paid to the development of lead-free halide perovskites. Most of the present high-performance photocatalysts and devices are based on lead halide perovskites; however, the toxicity of lead creates serious environmental concerns. To this end, tin-based and double halide perovskites[93] with comparable photophysical properties could be explored as alternatives. In summary, tremendous efforts have been made to enable halide perovskites to be useful for solar-to-chemical fuel conversion. In this review, we have summarized and discussed strategies established for fabricating halide perovskites for utilization in photocatalytic particle-suspension systems, photoelectrode thin-film systems, and photovoltaic-(photo)electrocatalytic tandem systems that target water splitting, HI splitting, and CO$_2$ reduction reactions. The future of halide perovskites in those applications is promising but will depend on discovering new and stable perovskite materials, developing protective and functional shells and layers, and designing suitable reaction solution systems as well as optimized tandem device configurations.

Acknowledgements

Conflict of Interest

The authors declare no conflict of interest.

Keywords

[1] P. De Luna, C. Hahn, D. Higgins, S. A. Jaffer, T. F. Jaramillo, E. H. Sargent, *Science* **2019**, *364*, eaav3506.

[2] X. Chen, S. Shen, L. Guo, S. S. Mao, *Chem. Rev.* **2010**, *110*, 6503.

[3] S. Shen, J. Chen, M. Wang, X. Sheng, X. Chen, X. Feng, S. S. Mao, *Prog. Mater. Sci.* **2018**, *98*, 299.

[4] K. Sun, S. Shen, Y. Liang, P. E. Burrows, S. S. Mao, D. Wang, *Chem. Rev.* **2014**, *114*, 8662.

[5] J. L. White, M. F. Baruch, J. E. Pander Iii, Y. Hu, I. C. Fortmeyer, J. E. Park, T. Zhang, K. Liao, J. Gu, Y. Yan, T. W. Shaw, E. Abelev, A. B. Bocarsly, *Chem. Rev.* **2015**, *115*, 12888.

[6] O. S. Bushuyev, P. De Luna, C. T. Dinh, L. Tao, G. Saur, J. van de Lagemaat, S. O. Kelley, E. H. Sargent, *Joule* **2018**, *2*, 825.

[7] N. Zhang, R. Long, C. Gao, Y. Xiong, *Sci. China Mater.* **2018**, *61*, 771.

[8] J. Luo, J.-H. Im, M. T. Mayer, M. Schreier, M. K. Nazeeruddin, N.-G. Park, S. D. Tilley, H. J. Fan, M. Grätzel, *Science* **2014**, *345*, 1593.

[9] C.-T. Dinh, T. Burdyny, M. G. Kibria, A. Seifitokaldani, C. M. Gabardo, F. P. García de Arquer, A. Kiani, J. P. Edwards, P. De Luna, O. S. Bushuyev, C. Zou, R. Quintero-Bermudez, Y. Pang, D. Sinton, E. H. Sargent, *Science* **2018**, *360*, 783.

[10] K. Sivula, R. van de Krol, *Nat. Rev. Mater.* **2016**, *1*, 15010.

[11] P. V. Kamat, *Acc. Chem. Res.* **2017**, *50*, 527.

[12] A. Kojima, K. Teshima, Y. Shirai, T. Miyasaka, *J. Am. Chem. Soc.* **2009**, *131*, 6050.

[13] D. Shi, V. Adinolfi, R. Comin, M. Yuan, E. Alarousu, A. Buin, Y. Chen, S. Hoogland, A. Rothenberger, K. Katsiev, Y. Losovyj, X. Zhang, P. A. Dowben, O. F. Mohammed, E. H. Sargent, O. M. Bakr, *Science* **2015**, *347*, 519.

[14] Y. Yang, Y. Yan, M. Yang, S. Choi, K. Zhu, J. M. Luther, M. C. Beard, *Nat. Commun.* **2015**, *6*, 7961.

[15] G. Xing, N. Mathews, S. Sun, S. S. Lim, Y. M. Lam, M. Grätzel, S. Mhaisalkar, T. C. Sum, *Science* **2013**, *342*, 344.

[16] A. A. Zhumekenov, M. I. Saidaminov, M. A. Haque, E. Alarousu, S. P. Sarmah, B. Murali, I. Dursun, X.-H. Miao, A. L. Abdelhady, T. Wu, O. F. Mohammed, O. M. Bakr, *ACS Energy Lett.* **2016**, *1*, 32.

[17] E. Alarousu, A. M. El-Zohry, J. Yin, A. A. Zhumekenov, C. Yang, E. Alhabshi, I. Gereige, A. AlSaggaf, A. V. Malko, O. M. Bakr, O. F. Mohammed, *J. Phys. Chem. Lett.* **2017**, *8*, 4386.

[18] J. Liu, K. Song, Y. Shin, X. Liu, J. Chen, K. X. Yao, J. Pan, C. Yang, J. Yin, L.-J. Xu, H. Yang, A. M. El-Zohry, B. Xin, S. Mitra, M. N. Hedhili, I. S. Roqan, O. F. Mohammed, Y. Han, O. M. Bakr, *Chem. Mater.* **2019**, *31*, 6642.

[19] S. De Wolf, J. Holovsky, S. J. Moon, P. Loper, B. Niesen, M. Ledinsky, F. J. Haug, J. H. Yum, C. Ballif, *J. Phys. Chem. Lett.* **2014**, *5*, 1035.

[20] Y. Fu, H. Zhu, J. Chen, M. P. Hautzinger, X. Y. Zhu, S. Jin, *Nat. Rev. Mater.* **2019**, *4*, 169.

[21] M. V. Kovalenko, L. Protesescu, M. I. Bodnarchuk, *Science* **2017**, *358*, 745.

[22] Y. Fu, F. Meng, M. B. Rowley, B. J. Thompson, M. J. Shearer, D. Ma, R. J. Hamers, J. C. Wright, S. Jin, *J. Am. Chem. Soc.* **2015**, *137*, 5810.

[23] Research Cell Efficiency Records, http://www.nrel.gov/pv/ (accessed: September 2019).

[24] Z. Chen, Q. Dong, Y. Liu, C. Bao, Y. Fang, Y. Lin, S. Tang, Q. Wang, X. Xiao, Y. Bai, Y. Deng, J. Huang, *Nat. Commun.* **2017**, *8*, 1890.

[25] A. O. El-Ballouli, O. M. Bakr, O. F. Mohammed, *Chem. Mater.* **2019**, *31*, 6387.

[26] H. M. Zhu, Y. P. Fu, F. Meng, X. X. Wu, Z. Z. Gong, Q. Ding, M. V. Gustafsson, M. T. Trinh, S. Jin, X.-Y. Zhu, *Nat. Mater.* **2015**, *14*, 636.

[27] Y. Fu, H. Zhu, C. C. Stoumpos, Q. Ding, J. Wang, M. G. Kanatzidis, X. Zhu, S. Jin, *ACS Nano* **2016**, *10*, 7963.

[28] Y. Cao, N. Wang, H. Tian, J. Guo, Y. Wei, H. Chen, Y. Miao, W. Zou, K. Pan, Y. He, H. Cao, Y. Ke, M. Xu, Y. Wang, M. Yang, K. Du, Z. Fu, D. Kong, D. Dai, Y. Jin, G. Li, H. Li, Q. Peng, J. Wang, W. Huang, *Nature* **2018**, *562*, 249.

[29] K. Lin, J. Xing, L. N. Quan, F. P. G. de Arquer, X. Gong, J. Lu, L. Xie, W. Zhao, D. Zhang, C. Yan, W. Li, X. Liu, Y. Lu, J. Kirman, E. H. Sargent, Q. Xiong, Z. Wei, *Nature* **2018**, *562*, 245.

[30] J. Luo, X. Wang, S. Li, J. Liu, Y. Guo, G. Niu, L. Yao, Y. Fu, L. Gao, Q. Dong, C. Zhao, M. Leng, F. Ma, W. Liang, L. Wang, S. Jin, J. Han, L. Zhang, J. Etheridge, J. Wang, Y. Yan, E. H. Sargent, J. Tang, *Nature* **2018**, *563*, 541.

[31] L. T. Dou, Y. Yang, J. B. You, Z. R. Hong, W. H. Chang, G. Li, Y. Yang, *Nat. Commun.* **2014**, *5*, 5404.

[32] W. Wei, Y. Zhang, Q. Xu, H. Wei, Y. Fang, Q. Wang, Y. Deng, T. Li, A. Gruverman, L. Cao, J. Huang, *Nat. Photonics* **2017**, *11*, 315.

[33] Q. Chen, J. Wu, X. Ou, B. Huang, J. Almutlaq, A. A. Zhumekenov, X. Guan, S. Han, L. Liang, Z. Yi, J. Li, X. Xie, Y. Wang, Y. Li, D. Fan, D. B. L. Teh, A. H. All, O. F. Mohammed, O. M. Bakr, T. Wu, M. Bettinelli, H. Yang, W. Huang, X. Liu, *Nature* **2018**, *561*, 88.

[34] Y. Zhang, R. Sun, X. Ou, K. Fu, Q. Chen, Y. Ding, L.-J. Xu, L. Liu, Y. Han, A. V. Malko, X. Liu, H. Yang, O. M. Bakr, H. Liu, O. F. Mohammed, *ACS Nano* **2019**, *13*, 2520.

[35] Y. Zhou, Y. Zhao, *Energy Environ. Sci.* **2019**, *12*, 1495.

[36] Y. F. Xu, M. Z. Yang, B. X. Chen, X. D. Wang, H. Y. Chen, D. B. Kuang, C. Y. Su, *J. Am. Chem. Soc.* **2017**, *139*, 5660.

[37] M. Crespo-Quesada, L. M. Pazos-Outon, J. Warnan, M. F. Kuehnel, R. H. Friend, E. Reisner, *Nat. Commun.* **2016**, *7*, 12555.

[38] J. Chen, J. Yin, X. Zheng, H. Ait Ahsaine, Y. Zhou, C. Dong, O. F. Mohammed, K. Takanabe, O. M. Bakr, *ACS Energy Lett.* **2019**, *4*, 1279.

[39] A. J. Bard, *J. Photochem.* **1979**, *10*, 59.

[40] A. Fujishima, K. Honda, *Nature* **1972**, *238*, 37.

[41] W.-Q. Wu, Z. Yang, P. N. Rudd, Y. Shao, X. Dai, H. Wei, J. Zhao, Y. Fang, Q. Wang, Y. Liu, Y. Deng, X. Xiao, Y. Feng, J. Huang, *Sci. Adv.* **2019**, *5*, eaav8925.

[42] S. Yang, Y. Wang, P. Liu, Y.-B. Cheng, H. J. Zhao, H. G. Yang, *Nat. Energy* **2016**, *1*, 15016.

[43] D. Ju, X. Zheng, J. Liu, Y. Chen, J. Zhang, B. Cao, H. Xiao, O. F. Mohammed, O. M. Bakr, X. Tao, *Angew. Chem., Int. Ed.* **2018**, *57*, 14868.

[44] X. Yang, L.-F. Ma, D. Yan, *Chem. Sci.* **2019**, *10*, 4567.

[45] Z.-J. Li, E. Hofman, J. Li, A. H. Davis, C.-H. Tung, L.-Z. Wu, W. Zheng, *Adv. Funct. Mater.* **2018**, *28*, 1704288.

[46] Z.-C. Kong, J.-F. Liao, Y.-J. Dong, Y.-F. Xu, H.-Y. Chen, D.-B. Kuang, C.-Y. Su, *ACS Energy Lett.* **2018**, *3*, 2656.

[47] Q. Zhong, M. Cao, H. Hu, D. Yang, M. Chen, P. Li, L. Wu, Q. Zhang, *ACS Nano* **2018**, *12*, 8579.

[48] A. Loiudice, S. Saris, E. Oveisi, D. T. L. Alexander, R. Buonsanti, *Angew. Chem., Int. Ed.* **2017**, *56*, 10696.

[49] A. Loiudice, M. Strach, S. Saris, D. Chernyshov, R. Buonsanti, *J. Am. Chem. Soc.* **2019**, *141*, 8254.

[50] S. Park, W. J. Chang, C. W. Lee, S. Park, H.-Y. Ahn, K. T. Nam, *Nat. Energy* **2017**, *2*, 16185.

[51] Y. Wu, P. Wang, X. Zhu, Q. Zhang, Z. Wang, Y. Liu, G. Zou, Y. Dai, M. H. Whangbo, B. Huang, *Adv. Mater.* **2018**, *30*, 1704342.

[52] Y. Wu, P. Wang, Z. Guan, J. Liu, Z. Wang, Z. Zheng, S. Jin, Y. Dai, M.-H. Whangbo, B. Huang, *ACS Catal.* **2018**, *8*, 10349.

[53] Z. Guan, Y. Wu, P. Wang, Q. Zhang, Z. Wang, Z. Zheng, Y. Liu, Y. Dai, M.-H. Whangbo, B. Huang, *Appl. Catal., B* **2019**, *245*, 522.

[54] H. Wang, X. Wang, R. Chen, H. Zhang, X. Wang, J. Wang, J. Zhang, L. Mu, K. Wu, F. Fan, X. Zong, C. Li, *ACS Energy Lett.* **2019**, *4*, 40.

[55] L. Zhou, Y. F. Xu, B. X. Chen, D. B. Kuang, C. Y. Su, *Small* **2018**, *14*, 1703762.

[56] J. Hou, S. Cao, Y. Wu, Z. Gao, F. Liang, Y. Sun, Z. Lin, L. Sun, *Chem. - Eur. J.* **2017**, *23*, 9481.

[57] M. Ou, W. Tu, S. Yin, W. Xing, S. Wu, H. Wang, S. Wan, Q. Zhong, R. Xu, *Angew. Chem., Int. Ed.* **2018**, *57*, 13570.

[58] L.-Y. Wu, Y.-F. Mu, X.-X. Guo, W. Zhang, Z.-M. Zhang, M. Zhang, T.-B. Lu, *Angew. Chem., Int. Ed.* **2019**, *58*, 9491.

[59] P. V. Kamat, S. Jin, *ACS Energy Lett.* **2018**, *3*, 622.

[60] S. Wan, M. Ou, Q. Zhong, X. Wang, *Chem. Eng. J.* **2019**, *358*, 1287.

[61] P. Da, M. Cha, L. Sun, Y. Wu, Z. S. Wang, G. Zheng, *Nano Lett.* **2015**, *15*, 3452.

[62] H. Zhang, Z. Yang, W. Yu, H. Wang, W. Ma, X. Zong, C. Li, *Adv. Energy Mater.* **2018**, *8*, 1800795.

[63] I. Poli, U. Hintermair, M. Regue, S. Kumar, E. V. Sackville, J. Baker, T. M. Watson, S. Eslava, P. J. Cameron, *Nat. Commun.* **2019**, *10*, 2097.

[64] C. Wang, S. Yang, X. Chen, T. Wen, H. G. Yang, *J. Mater. Chem. A* **2017**, *5*, 910.

[65] M. T. Hoang, N. D. Pham, J. H. Han, J. M. Gardner, I. Oh, *ACS Appl. Mater. Interfaces* **2016**, *8*, 11904.

[66] S. Nam, C. T. K. Mai, I. Oh, *ACS Appl. Mater. Interfaces* **2018**, *10*, 14659.

[67] R. Tao, Z. Sun, F. Li, W. Fang, L. Xu, *ACS Appl. Energy Mater.* **2019**, *2*, 1969.

[68] V. Andrei, R. L. Z. Hoye, M. Crespo-Quesada, M. Bajada, S. Ahmad, M. De Volder, R. Friend, E. Reisner, *Adv. Energy Mater.* **2018**, *8*, 1801403.

[69] L.-F. Gao, W.-J. Luo, Y.-F. Yao, Z.-G. Zou, *Chem. Commun.* **2018**, *54*, 11459.

[70] S. Ahmad, A. Sadhanala, R. L. Z. Hoye, V. Andrei, M. H. Modarres, B. Zhao, J. Ronge, R. Friend, M. De Volder, *ACS Appl. Mater. Interfaces* **2019**, *11*, 23198.

[71] I. S. Kim, M. J. Pellin, A. B. F. Martinson, *ACS Energy Lett.* **2019**, *4*, 293.

[72] Y. S. Chen, J. S. Manser, P. V. Kamat, *J. Am. Chem. Soc.* **2015**, *137*, 974.

[73] J. H. Kim, Y. Jo, J. H. Kim, J. W. Jang, H. J. Kang, Y. H. Lee, D. S. Kim, Y. Jun, J. S. Lee, *ACS Nano* **2015**, *9*, 11820.

[74] Gurudayal, D. Sabba, M. H. Kumar, L. H. Wong, J. Barber, M. Grätzel, N. Mathews, *Nano Lett.* **2015**, *15*, 3833.

[75] P. Dias, M. Schreier, S. D. Tilley, J. Luo, J. Azevedo, L. Andrade, D. Bi, A. Hagfeldt, A. Mendes, M. Grätzel, M. T. Mayer, *Adv. Energy Mater.* **2015**, *5*, 1501537.

[76] S. Xiao, C. Hu, H. Lin, X. Meng, T. Zhang, Y. Yang, Y. Qu, K. Yan, J. Xu, Y. Qiu, S. Yang, *J. Mater. Chem. A* **2017**, *5*, 19091.

[77] J. Luo, Z. Li, S. Nishiwaki, M. Schreier, M. T. Mayer, P. Cendula, Y. H. Lee, K. Fu, A. Cao, M. K. Nazeeruddin, Y. E. Romanyuk, S. Buecheler, S. D. Tilley, L. H. Wong, A. N. Tiwari, M. Grätzel, *Adv. Energy Mater.* **2015**, *5*, 1501520.

[78] Y. Qiu, W. Liu, W. Chen, G. Zhou, P.-C. Hsu, R. Zhang, Z. Liang, S. Fan, Y. Zhang, Y. Cui, *Sci. Adv.* **2016**, *2*, e1501764.

[79] G. Segev, J. W. Beeman, J. B. Greenblatt, I. D. Sharp, *Nat. Mater.* **2018**, *17*, 1115.

[80] Y. J. Jang, I. Jeong, J. Lee, M. J. Ko, J. S. Lee, *ACS Nano* **2016**, *10*, 6980.

[81] X. Zhang, B. Zhang, K. Cao, J. Brillet, J. Chen, M. Wang, Y. Shen, *J. Mater. Chem. A* **2015**, *3*, 21630.

[82] B. Sun, T. Shi, Z. Liu, Z. Tang, J. Zhou, G. Liao, *RSC Adv.* **2016**, *6*, 110120.

[83] J. H. Kim, Y. H. Jo, J. S. Lee, *Nanoscale* **2016**, *8*, 17623.

[84] Gurudayal, R. A. John, P. P. Boix, C. Yi, C. Shi, M. C. Scott, S. A. Veldhuis, A. M. Minor, S. M. Zakeeruddin, L. H. Wong, M. Grätzel, N. Mathews, *ChemSusChem* **2017**, *10*, 2449.

[85] J. H. Baek, B. J. Kim, G. S. Han, S. W. Hwang, D. R. Kim, I. S. Cho, H. S. Jung, *ACS Appl. Mater. Interfaces* **2017**, *9*, 1479.

[86] S. Wang, P. Chen, Y. Bai, J. H. Yun, G. Liu, L. Wang, *Adv. Mater.* **2018**, *30*, 1800486.

[87] X. Liu, Y. Wang, X. Cui, M. Zhang, B. Wang, M. Rager, Z. Shu, Y. Yang, Z. Li, Z. Lin, *J. Mater. Chem. A* **2019**, *7*, 165.

[88] J. Luo, D. A. Vermaas, D. Bi, A. Hagfeldt, W. A. Smith, M. Grätzel, *Adv. Energy Mater.* **2016**, *6*, 1600100.

[89] M. Schreier, L. Curvat, F. Giordano, L. Steier, A. Abate, S. M. Zakeeruddin, J. Luo, M. T. Mayer, M. Grätzel, *Nat. Commun.* **2015**, *6*, 7326.

[90] X. Zhu, Y. Lin, Y. Sun, M. C. Beard, Y. Yan, *J. Am. Chem. Soc.* **2019**, *141*, 733.

[91] H. Huang, H. Yuan, K. P. F. Janssen, G. Solís-Fernández, Y. Wang, C. Y. X. Tan, D. Jonckheere, E. Debroye, J. Long, J. Hendrix, J. Hofkens, J. A. Steele, M. B. J. Roeffaers, *ACS Energy Lett.* **2018**, *3*, 755.

[92] H. Huang, H. Yuan, J. Zhao, G. Solís-Fernández, C. Zhou, J. W. Seo, J. Hendrix, E. Debroye, J. A. Steele, J. Hofkens, J. Long, M. B. J. Roeffaers, *ACS Energy Lett.* **2019**, *4*, 203.

[93] G. Volonakis, F. Giustino, *Appl. Phys. Lett.* **2018**, *112*, 243901.